Sharp-Interface Simulations of Heat-Driven Flows with Marangoni Effect

Johannes L. Pieper

Institute of Aerodynamics and Fluid Mechanics
Technical University of Munich
Garching, Germany
Pieper@mytum.de

Felix S. Schranner

Institute of Aerodynamics and Fluid Mechanics
Technical University of Munich
Garching, Germany
schranne@tum.de

Gurvan Hermange

Institute of Aerodynamics and Fluid Mechanics
Technical University of Munich
Garching, Germany
gurvan.hermange@gmail.com

Nikolaus A. Adams

Institute of Aerodynamics and Fluid Mechanics
Technical University of Munich
Garching, Germany
Nikolaus.Adams@tum.de

Abstract

A method to account for the effect of interfacial surfactant concentration on multi-phase flows has been proposed by Schranner & Adams (2016). The therein validated method builds up on the the sharp-interface method of Hu *et al.* (2006). This work advances the method to simulate and analyse configurations of industrial applicability. In the majority of these configurations temperature gradients, commonly due to local heat sources or sinks, are the dominant cause of the Marangoni flow. In order to account for the Marangoni effect properly, the temperature distribution within the two-phase flows under consideration has to be known. In this work, two numerical approaches for the calculation of the temperature are presented and evaluated. In the first approach the temperature transport equation, realized as a scalar transport equation, is coupled to the finite volume algorithm of Schranner & Adams (2016). The underlying method for the second approach is the weakly compressible high-resolution approach for incompressible flows (Schranner *et al.* (2013)), which is generalized to compressible and incompressible flows. The extension to multi-phase flows with discontinuous phases is formulated in this work. The approaches are evaluated and compared on basis of the test flow proposed by Pendse & Esmaeeli (2010). It is sufficiently complex in its evolution, yet simple in its set-up and permits comparison to an analytical reference solution. The application of the methods to further thermocapillary flows is pursued. Both methods are robust and correctly predict the evolution of the Marangoni flows and temperature fields. Numerical experiments indicate that the passive scalar method is faster than the energy equation method. Yet, for two-phase flows with fluids of very diverse properties the energy equation method is more accurate.

Introduction

In many classical two-phase flows, such as viscous fingering (Matar & Troian (1999)), drop break-up and coalescence (Leal (2004)), tip-streaming (Bruijn (1993)), and buoyancy-driven bubble-motion (Fdhila & Duineveld (1996)), the effects of locally variable surface tension are significant. The causes are inhomogeneously distributed interfacial surfactants and temperature gradients.

The accurate and concurrently robust two-phase flow simulation of immiscible fluids with large density and viscosity ratios in combination with resolved interface dynamics can be numerically challenging. Hu *et al.* (2006) have developed a fully conservative, Eulerian, level-set based sharp-interface method (SIM) to simulate immiscible, compressible flows. The sharp-interface framework has demonstrated to accurately predict two-phase flows, with each phase obeying different equations of state, and large density and viscosity ratios (Lauer *et al.* (2012); Schranner *et al.* (2016)). A viscous extension of the SIM for incompressible two-fluid flows is due to Luo *et al.* (2015). A robust, more accurate, simpler and easy to implement further-development of the SIM that incorporates inviscid, viscous, capillary and Marangoni interfacial stresses is due to Schranner & Adams (2016). Generally, the SIM has demonstrated to be a reliable and simple approach to capture multi-fluid interfaces robustly even for complex interface topology changes (Luo *et al.* (2015); Hu *et al.* (2006); Lauer *et al.* (2012); Schranner *et al.* (2016)).

To account for interfacial surfactant transport a method has been developed and applied for the diffuse interface approach by Teigen *et al.* (2011), Adalsteinsson & Sethian (2003), and Xu & Zhao (2003). It has been improved in terms of accuracy, surfactant mass conservation and computational efficiency by Schranner & Adams (2016), employing the sharp-interface methodology. To allow for the simulation of temperature-gradient driven Marangoni flows, the transport of mass, momentum and energy within each phase and across the interface needs to be considered appropriately. Based on the accurate interfacial temperature distribution, the local capillary and Marangoni stresses as well as their contribution to the momentum and energy balance of the involved fluids can be computed straightforwardly. This generalization is pursued within the scope of this work. Therefore, two numerical approaches for advancing the temperature within the phases and exchanging energy across the interface are presented. They are evaluated on basis of a selection of test flows. Furthermore, the industrial application are sought.

Basic Concepts

The finite-volume algorithm of Schranner *et al.* (2013) for weakly compressible turbulent and non-turbulent single-phase flows, further-developed to multi-phase configurations with capillary and Marangoni effects Schranner & Adams (2016) is the underlying numerical method. For incompressible flows the energy equation is decoupled from the transport of mass and momentum Panton (1984) and becomes obsolete. Yet, it is not obsolete if internal energy or temperature distributions are of interest.

Passive scalar temperature transport equation (PS)

For incompressible multi-phase flows with temperature gradients and negligible temporal pressure fluctuations the temperature equation

$$\rho c_p \left(\frac{\partial T}{\partial t} + \mathbf{u} \cdot \nabla T \right) = \nabla \lambda \cdot \nabla T + \lambda \triangle T - \\ - \frac{2}{3} \mu \left(\nabla \cdot \mathbf{u} \right)^2 + 2\mu \left((\nabla \mathbf{u}) : (\nabla \mathbf{u}) \right) + \beta T \mathbf{u} \nabla p + \dot{\omega} \tag{1}$$

holds within the two-fluid domain $\Omega = \Omega^{\xi_1} \cup \Omega^{\xi_2}$. The heat capacity c_p, coefficient of thermal expansion β, thermal conductivity λ, dynamic viscosity $\mu = \rho\nu$ are material properties of the fluids ξ_1 and ξ_2. Numerically, within the multi-fluid cells, which are those cells containing both fluids, the material properties are determined from the volume fractions $\zeta^{\xi_i}(t) = \frac{1}{V} \int\limits_{\Omega \cap \Omega^{\xi_i}} dV$ of the fluid phases ξ_i and the individual fluid properties: e.g. $c_p = (\zeta c_p)^{\xi_1} + (\zeta c_p)^{\xi_2}$. The derivatives of Eq. (1) are approximated with 4^{th}-order central (LHS: 1^{st} term, RHS: 1^{st}, 2^{nd}, 3^{rd} , 4^{th} term) and 5^{th}-order upwind-biased (LHS: 2^{nd} term, RHS: 5^{th} term) finite difference schemes, respectively. Note, however, from numerical experiments we find that the order of convergence is independent from the choice of the order for the central differences, thus due to the order of accuracy of the scheme for fluid transport. The 6^{th} term of Eq. (1) defines volume and area sources. To consider an area-distributed heat source (AHS) the power of a radiative heat source P is considered to act uniformly on a certain area AIF_{tot}. The product with the ratio of interface-area $AIF_{[i,j,k]}$ to volume $V_{[i,j,k]}$ of a cell $[i,j,k]$ is the heat added to each cell at the interface: $\dot{\omega} = \frac{P}{AIF_{tot}} \frac{AIF_{[i,j,k]}}{V_{[i,j,k]}}$.

Energy equation method (EEM)

The method of Schranner & Adams (2016) is extended to incorporate the energy equation for compressible as well as weakly compressible flows, see also Schranner (2017). Hence, within each fluid phase the transport equations for the conservative states $\mathbf{U} = (\rho, \rho\mathbf{u}, \rho e_t)$ are solved seperately. $e_t = e_{kin} + e_i$. By considering the interface-interaction flux in each multi-fluid cell

$$\mathbf{X}^{\xi_i} = \{0, \mathbf{X}^{M,\xi_i}, \mathbf{X}^{E,\xi_i}\} \tag{2}$$

the two subdomains Ω^{ξ_i} containing one of the fluids ξ_i are coupled and the system is globally conservative. The momentum flux is: $\mathbf{X}^{M,\xi_i} = \{\mathbf{X}^{\perp,\xi_i} + \mathbf{X}^{\parallel,\xi_i}\}$ (Schranner & Adams (2016)). In contrast to Schranner (2017) conductive heat transfer is also considered in this work. Thus, the interfacial energy flux is

$$\mathbf{X}^{E,\xi_i} = \mathbf{X}^{M,\xi_i} \cdot \mathbf{u}_I^{\xi_i} + \mathbf{q}_I \cdot \mathbf{n}_I^{\xi_i}. \tag{3}$$

Thereby, the interface heat flux is

$$\mathbf{q}_I = q_{I,\alpha} = -\lambda_{I,\alpha} \mathfrak{D}(T)_{I,\alpha} \tag{4}$$

with $\alpha = 1,2,3$ denoting the Cartesian directions. Numerically, the temperature gradient across the interface in direction α, denoted as $\mathfrak{D}(T)_{I,\alpha}$, is approximated with a 4^{th}-order central difference. The stencil is constructed of $T = \{(\zeta T)^{\xi_1} + (\zeta T)^{\xi_2}\}$. To account for the discontinuous λ within interface cells, let

$$\lambda_{I,\alpha} = \frac{1}{\mathfrak{D}\left(\int^{x_\alpha} \frac{1}{\lambda(u)} \mathrm{d}u \right)}. \tag{5}$$

The order of the approximation of $\mathfrak{D}$ of Eq. (5) is consistent with the order of $\mathfrak{D}(T)_{I,\alpha}$. The interface temperature T_I is obtained from $e_i = c_p T_I$.

Temperature dependent material properties

Temperature dependencies of the material properties are considered. For incompressible or weakly compressible fluids, the Boussinesq approximation is used to account for a temperature dependent density in the buoyant force, modeled as a source term:

$$\rho = \rho_{ref} \cdot \left(1 - \beta_T \left(T - T_{ref}\right)\right), \tag{6}$$

where β_T is the coefficient of thermal expansion.
The temperature dependent surface-tension σ is modeled with a linear Langmuir constitutive equation:

$$\sigma(T) = \sigma_{ref} + \frac{\partial \sigma}{\partial T} \left(T - T_{ref}\right). \tag{7}$$

σ_{ref} is the surface tension coefficient at a reference temperature T_{ref}. These as well as the temperature gradient $\frac{\partial \sigma}{\partial T}$ are constant and material-specific.
To consider solidification and melting phase changes the dynamic viscosity is considered constant and relatively high for temperatures lower than a specific the melting temperature T_S. For higher temperatures, the dynamic viscosity obeys an Arrhenius function. Continuous transition is achieved by means of a Heaviside function.

$$\mu(T) = \begin{cases} \mu_{max}, & T < T_S - 2 \cdot \delta T \\ (\mu_{max} - \mu(T_S)) \cdot & \\ (1 - H(T - T_S + \delta T, \delta T)), & T_S - 2 \cdot \delta T \leq T_S \\ \mu_0 \cdot \exp\left(\frac{E}{T - T_S}\right), & T \geq T_S. \end{cases} \tag{8}$$

The temperature dependency of the specific heat capacity c_p includes a normally distributed latent heat h_S around the melting point, the width is ΔT:

$$c_p(T) = c_p + \frac{\exp\left(-\left(\frac{T - T_S}{\Delta T}\right)^2\right)}{\sqrt{\pi} \Delta T} \cdot h_S. \tag{9}$$

Thermocapillary Flow

To validate the two models and verify their implementation a thermocapillary driven creeping flow with two superimposed planar fluids is considered, see Pendse & Esmaeeli (2010). The analytical solutions for the temperature T field, and the velocities u and v are available. The geometrical set-up is shown in figure 1.

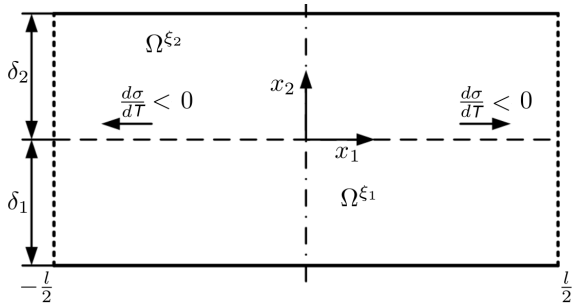

Figure 1. Geometrical Set-up for thermocapillary flow.

$\delta_1 = \delta_2 = 1.0$ and $l = 4\delta_1$ are used. The boundary condition are periodic in x_1-direction. In x_2-directions a no-slip condition is assumed. The uniform temperature $T(x_1, \delta_2) = T_c$ is imposed at the top boundary. Along the bottom boundary a sinusoidal temperature distribution with $T(x_1, -\delta_1) = T_h + \Delta T \cos(\frac{2\pi}{l} x_1)$ is assumed. $T_h = 20$, $\Delta T = 4$, $T_c = 10$. The steady-state solution may be found in Pendse & Esmaeeli (2010) or Schranner & Adams (2016). The kinematic viscosities are $\nu^{\xi_1} = \nu^{\xi_2} = 0.2$. Both fluids obey the Tait equation of state, with $\gamma = 1.000001$. The speed of sound depends on the density. For fluids with $\rho = 1.0$ the speed of sound is $a = 10$, for fluids with $\rho = 1000$ the speed of sound is $a = 1.0$. Moreover, $\frac{\partial \sigma}{\partial T} = -5 \cdot 10^{-4}$ and $\sigma_0 = 0.03$ at $T_{ref} = 10$. Four different cases are considered. For the upper fluid $\rho^{\xi_2} = 1.0$, $c^{\xi_2} = 2/3$ and $\lambda^{\xi_2} = 0.2$. The density, heat capacity and the thermal conductivity of the lower fluid are case-dependent:

- Case 1: $\rho^{\xi_1} = \rho^{\xi_2}$, $c^{\xi_1} = c^{\xi_2}$ and $\lambda^{\xi_1} = \lambda^{\xi_2}$,
- Case 2: $\rho^{\xi_1} = \rho^{\xi_2}$, $c^{\xi_1} = 5c^{\xi_2}$ and $\lambda^{\xi_1} = 5\lambda^{\xi_2}$,
- Case 3: $\rho^{\xi_1} = 1000\rho^{\xi_2}$, $c^{\xi_1} = c^{\xi_2}/1000$ and $\lambda^{\xi_1} = \lambda^{\xi_2}$,
- Case 4: $\rho^{\xi_1} = 1000\rho^{\xi_2}$, $c^{\xi_1} = c^{\xi_2}5/1000$ and $\lambda^{\xi_1} = 5\lambda^{\xi_2}$.

The reference length and velocity are $L_{ref} = \delta_1 = 1.0$ and $U_{ref} = \frac{|\frac{\partial\sigma}{\partial T}\Delta T|}{\mu^{\xi_1}}\frac{\delta_1}{l} = \frac{1}{400}$, respectively. Thus, one finds that the Reynolds, Marangoni, Peclet, capillary, and Weber numbers are $\mathrm{Re} = \frac{U_{ref}L_{ref}}{\nu^{\xi_2}} = 0.0125$, $\mathrm{Ma} = \frac{U_{ref}\rho^{\xi_2}c^{\xi_2}l}{\lambda^{\xi_2}} = \frac{1}{30}$, $\mathrm{Pe} = \frac{U_{ref}L_{ref}\rho^{\xi_2}c^{\xi_2}}{\lambda^{\xi_2}} = \frac{1}{120}$, $\mathrm{Ca} = \frac{\rho^{\xi_2}U_{ref}\nu^{\xi_2}}{\sigma_0} = \frac{1}{60}$ $\mathrm{We} = \frac{\rho^{\xi_2}U_{ref}^2L_{ref}}{\sigma_0} = \frac{1}{4800}$. These numbers comply $\mathrm{Re} << 1$, $\mathrm{Ca} << 1$ and $\mathrm{Ma} << 1$, hence the analytical solution of Pendse & Esmaeeli (2010) hold.

To evaluate the simulation, the L_∞- L_1- and L_2- absolut errors are evaluated. The absolute error norms are calculated for u, v and T

$$L_\infty = max_M\left(|\varepsilon|\right), \tag{10a}$$

$$L_1 = \int_{\Delta V}|\varepsilon|dV' \approx \sum_M\{|\varepsilon|\Delta V\}_{[i,j]}, \tag{10b}$$

$$L_2 = \left(\int_{\Delta V}|\varepsilon|^2dV'\right)^{1/2} \approx \left(\sum_M\{|\varepsilon|^2\Delta V\}_{[i,j]}\right)^{1/2}. \tag{10c}$$

The resolution Δx is reduced in five steps from 0.2 to 0.00625.

Case 1

The first case serves as a basic verification and validation configuration. The temperature and flow field is depicted in Fig. 2. Figure 3 shows the L_1 errors for the EEM and PS approaches. For both methods the results converge to the analytical solution independent from the chosen approach. Regarding T, L_1 is below 0.0149 for PS and 0.266 for EEM. The maximum error is lower than 0.02 for both methods at the largest resolution. The largest deviation of u and v, found on the interface, is $2.71\cdot10^{-5}$ (PS) and $3.74\cdot10^{-5}$ (EEM), $1.80\cdot10^{-5}$ (PS) and $1.74\cdot10^{-5}$ (EEM), respectively. With respect to the maximum velocities of $u_{max} = 3\cdot10^{-4}$ and $v_{max} = 6\cdot10^{-5}$ these values indicate good results even for the lowest resolution. Spatial refinement leads to a reduction in the errors. The convergence order is between 1.0 and 0.3 for the velocities, and $1.0 < L_1(T) < 1.6$ for T.

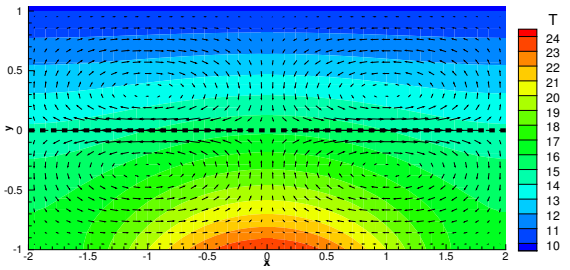

Figure 2. Results (PS) for Case 1 with $\Delta x \approx \frac{1}{20}$ at steady state, $t = 20$.

Case 2

The second case simulates two fluids with the same density and different thermal conductivities and capacities. This corresponds to a highly simplified model of a laser beam welding process, as air and metal have a large difference in their thermal conductivities and capacities. Figure 4 depicts the L_1 errors for the EEM and PS. L_2 and L_∞ are not shown for clarity. The simulation results for both methods are in a good agreement with the analytical solution. EEM leads to more accurate results than the results of PS. This is found from evaluating all three error norms.

A possible explanation may be that while the EEM calculates the

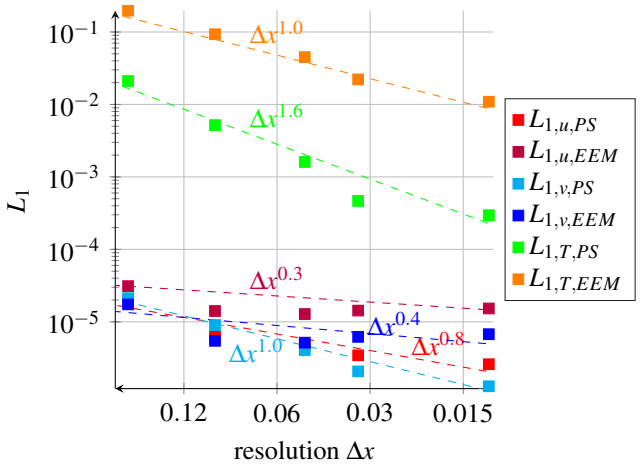

Figure 3. L_1 error norms for u , v and T for Case 1 with PS and EEM at steady state, $t = 20$.

energy for both fluids and models the heat flux across the sharp interface, the PS calculates the temperature for the entire domain without explicitly considering the interface. The deviations from the analytical solution are larger with the PS. Consequently, larger deviations in the temperature gradient are found which lead to different results of the flow velocities. The maximum velocities of the analytical solution are $u_{max,anly} \approx 5.60\cdot10^{-4}$ and $v_{max,anly} \approx 1.20\cdot10^{-4}$. The simulated maximum velocities are $u_{max,PS} \approx 5.75\cdot10^{-4}$, $v_{max,PS} \approx 1.24\cdot10^{-4}$, $u_{max,EEM} \approx 5.37\cdot10^{-4}$, $v_{max,EEM} \approx 1.16\cdot10^{-4}$ found at a mesh width of $\Delta x \approx 0.05$. The accuracy of the first case is not achieved for both methods. The temperature order of convergence is about 0.2 for PS and 1.0 for EEM.

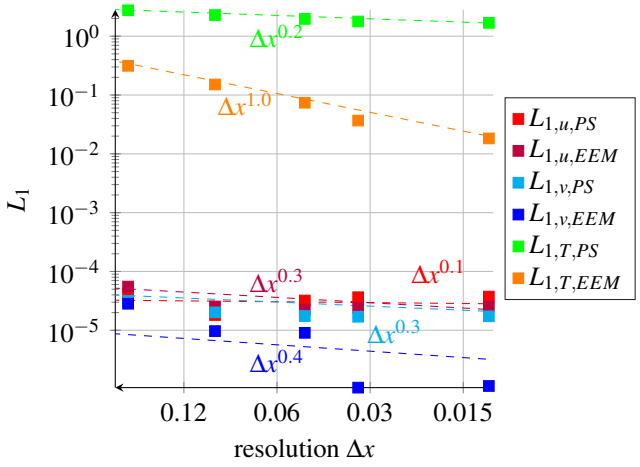

Figure 4. L_1 error norms for velocity u , v and temperature T for Case 2 with PS and EEM at steady state, $t = 20$.

Case 3

This case extends Case 1 by considering a density of 1000. Figure 5 depicts the L_1 errors for the temperature at different resolutions. The velocity contours are depicted in figure 6 The temperature distribution approaches the analytical solution well. The maximum errors, e.g. L_∞, are identical to Case 1 for both methods and same resolutions.

In the upper fluid, Ω^{ξ_2}, which has a lower density, significantly higher velocities are observed in the stationary state than in Ω^{ξ_1}

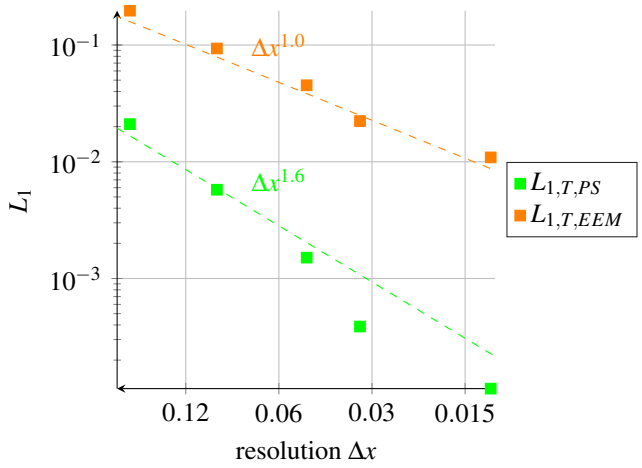

Figure 5. L_1 error norms for T for Case 3 with PS and EEM at steady state, $t = 20$.

independent from when employing EEM or PS.

According to Pendse & Esmaeeli (2010) the density has no influence on the solution as long as Re$<<1$, Ca$<<1$ and Ma$<<1$. The ratio of the two dynamic viscosities, which is reduced from 1 (Case 1) to 1000, has only an influence on the maximum velocity in the analytical solution. Pendse & Esmaeeli (2010) do not impose any restriction to the density ratios. The question is raised, at this venue, whether the analytical solution does or does not apply to combinations of fluids with very large density ratios, although the creeping flow conditions are fulfilled for one of the two fluid. Within ξ_1 (the lower fluid) $Ca = \frac{1000}{60}$ for Case 3, for Cases 1 and 2 it is $Ca = \frac{1}{60}$. Hence, ξ_1 cannot be considered a creeping flow, even though ξ_2 can.

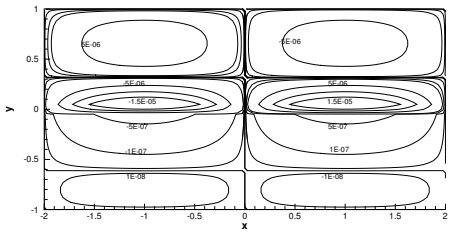

(a) u-velocity field

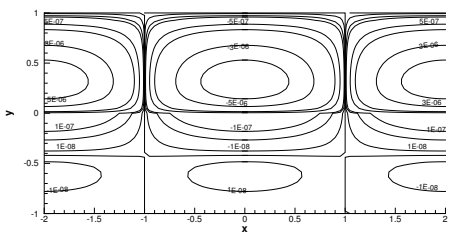

(b) v-velocity field

Figure 6. Velocities u and v with a density-ratio of 1000 at steady state, $t = 20$.

Case 4

Case 4 is a combination of Cases 2 and 3. It is a configuration that resembles laser beam welding better than the previous cases. Figure 7 depicts the L_1 temperature error norms for when employing EEM and PS. The temperature fields as well as the resolution dependent error norms are found to be identical to those of Case 2. The velocities are found to differ significantly from the analytical solution. A possible explanation is given for Case 3, which also holds for Case 4.

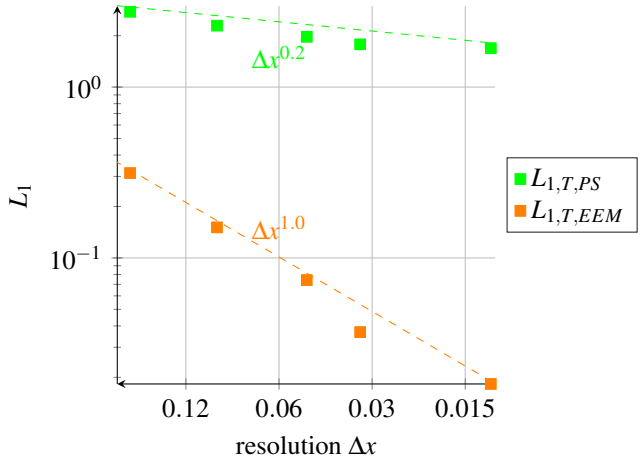

Figure 7. L_1 error norms for T for Case 4 with PS and EEM at steady state, $t = 20$.

Thermocapillary motion of a Drop

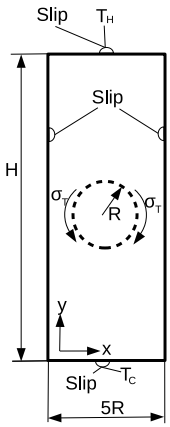

Figure 8. Principal sketch of the Set-up for Rising Bubble.

Another test case for the validation of the implemented equations is provided by Young *et al.* (1959), who have investigated the velocity of a two-dimensional rising drop. For this purpose, a drop with the radius R is set in a cylinder with the height L and the radius $5R$ (see figure 8). Furthermore, a linear temperature field is specified over the height of the cylinder. The temperature at the bottom of the cylinder is $T\,(y=0) = T_H$ and at the top $T\,(y=L) = T_C$. This results in a linear temperature profile. The surface tension changes linearly with the height according to the temperature distribution. For validation, the average ascent rate is calculated and compared to the ascent rate u_{YGB} according to Young *et al.* (1959). The empirically evaluated ascent rate is

$$u_{YGB} = \frac{2\left(\frac{\partial\sigma}{\partial T}\cdot\frac{T_H - T_C}{L}R - \Delta\rho g R^2\frac{\mu_1+\mu_2}{\mu_1}\right)}{9\mu_1 + 6\mu_2}. \qquad (11)$$

The average ascent rate of the simulated drop is determined by

$$\bar{u}_2 = \frac{1}{V_2}\int_{\Omega_2} u_2 dV = \frac{1}{V_2}\sum_M u_2 \zeta^{\xi_2} \Delta V, \tag{12}$$

where M is the number of cells, V_2 is the volume of the drop, and ζ^{ξ_2} is the volume fraction of the disperse phase. Furthermore, $R = 0.5$ and $L = 7.5R$. For the fluids, $\rho^{\xi_1} = \rho^{\xi_2} = 0.2$, $a^{\xi_1} = 5.0$, $a^{\xi_2} = 40$. The Tait equation of state holds for both fluids. The initial pressure for both fluids is equal to $p_0 = 0$. With the dynamic viscosity $\mu^{\xi_1} = \mu^{\xi_2} = 0.1$, $g = 0$, $\frac{\partial \sigma}{\partial T} = -1$ and the temperatures $T_C = 300$ and $T_H = 300.5$, a theoretical ascent rate of $u_{YGB} = \frac{4}{45}$ is obtained. Thus, the Reynolds number is Re$= \frac{8}{45}$. This configuration is simulated with EEM and PS. The results are nearly identical. For clarity, we only provide results for PS in Figs. 9, 10.

A convergence analysis is performed with a spatial resolution ranging from $\frac{2.5}{32}$ to $\frac{2.5}{256}$, four different refinement levels are simulated. For a resolution of $\Delta x = \frac{2.5}{128}$ the deviation from the theoretical ascent rate is already less than 1%. The results can be considered to be converged for a resolution of $\Delta x = \frac{2.5}{128}$ as these do not differ for a grid of $\Delta x = \frac{2.5}{256}$. The predicted ascent rates of the drop and the pressures agree well with the empirical solutions.

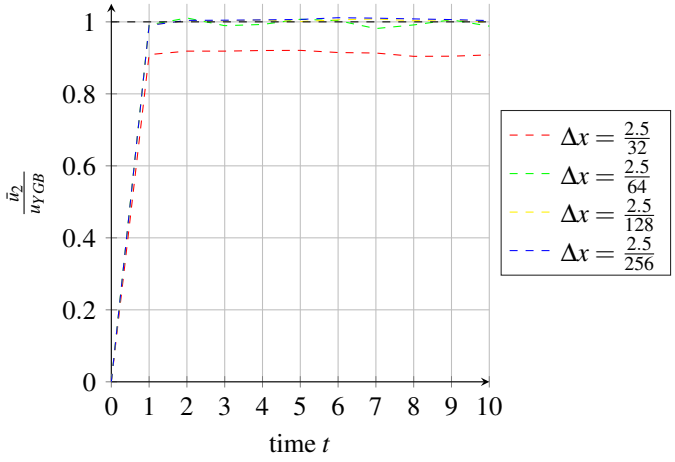

Figure 9. Normalised ascent velocity for different resolutions

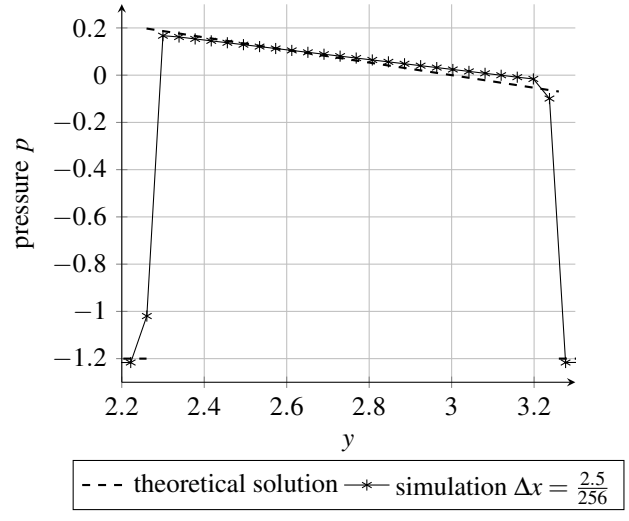

Figure 10. Simulated pressure at $x = 1.25$ and $t = 10$ compared to theoretically expected pressure

Application Example - Laserdeep-Welding

Based on Case 4, a simple set-up to simulate heat conduction welding is developed. Copper is chosen to be the welding material and air as the ambient gas. The geometrical set-up is $l = 0.001$ and $\delta_1 = \delta_2 = 0.00025$, comparable to figure 1. Moreover, $\rho^{\xi_2} = 1.19$, $c^{\xi_2} = 1004$, $\mu^{\xi_2} = 1.8485 \cdot 10^{-5}$ and $\lambda^{\xi_2} = 0.0262$, $\rho^{\xi_1} = 8960$, $c^{\xi_1} = 385$ and $\lambda^{\xi_1} = 394$. The latent heat of copper is $h_S^{\xi_1} = 207000$, it is distributed normally with $\Delta T = 25$ around the melting point $T_S^{\xi_1} = 1357$, see Eq. (9). The dynamic viscosity is modeled according to Eq. (8), $\mu_{max}^{\xi_1} = 100$, $\mu^{\xi_1}(T_S) = 0.0003$ and $E^{\xi_1} = 3666$. The heat source is a laser beam, modeled as an AHS. It acts within a small region with an focus diameter of $d_f = 0.0003$ and a powerdensity of $3 \cdot 10^9$. To account for thermal convection, $\rho(T)$ is modeled according to Eq. (6). To model the temperature dependent surface tension Eq. (7) holds. The set-up is shown in Figure 11. The feed

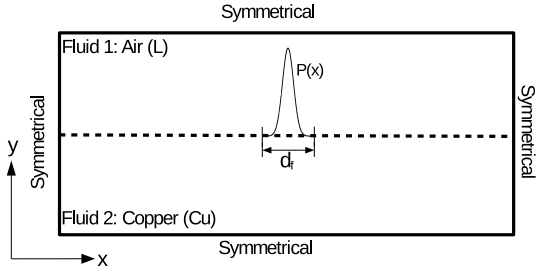

Figure 11. Geometrical setup of the laser welding configuration.

rate is zero in order to examine the convection in the molten pool. We simulate the initial heat-up process. The flow within the molten metal pool and air are visualized in Figs. 12 and 13, respectively. Note that the molten metal pool is the area enclosed by the $T = T_S$-line, the temperature within the enclosed area is higher than T_S. The two-dimensional model with the selected parameters shows that the melting temperature is reached after $3.5 \cdot 10^{-4} s$. A Marangoni flow develops, driving the liquid phase. The maximum velocities are observed at the interface where the melting temperature $T_S = 1357$ is reached. The comparably higher velocities in the air are due to the comparably low dynamic viscosity of the air.

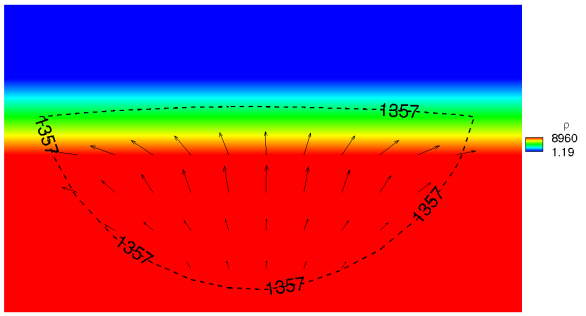

Figure 12. Fluid flows in molten metal pool at $t = 1.5 \cdot 10^{-3}$.

Conclusion

Two methods to simulate two-phase immiscible, incompressible flows with temperature dependent material properties have been presented. Both methods are applicable to simulate Marangoni flows with a sharp-interface. In the first method temperature is propagated as a passive scalar, multifluid cells are considered by mixing fluid properties, the transport equations of mass and momentum apply for the fluids in motion, the exchange of momentum across the interface couples the two phases. The second method employs the transport equations for mass, momentum and energy and couples the immiscible phases by means of interface-fluxes, modeling the

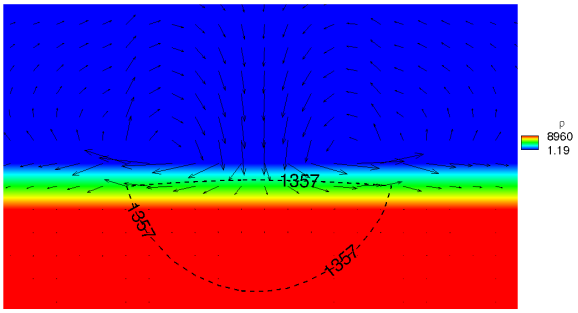

Figure 13. Fluid flow in ambient gas at $t = 1.5 \cdot 10^{-3}$.

exchange of momentum and energy across the interface. By comparing the results to analytical solutions of a selection of test flows the methods are verified and their implementations validated.

Both methods are robust and correctly predict the evolution of the Marangoni flows and temperature fields. The simulation results of a thermocapillary flow are in excellent agreement with analytical data for both methods. Numerical experiments indicate that the passive scalar method is faster than the energy equation method. Yet, for two-phase flows with fluids of very diverse properties the energy equation method is more accurate. As an industrial application example a two-dimensional base configuration of a laser beam welding process has been simulated.

Acknowledgment

We acknowledge the Deutsche Forschungsgemeinschaft (DFG) for funding. Felix S. Schranner is member of the TUM Graduate School. The Munich Centre of Advanced Computing (MAC) has provided the computational resources.

REFERENCES

Adalsteinsson, David & Sethian, J.A. 2003 Transport and diffusion of material quantities on propagating interfaces via level set methods. *Journal of Computational Physics* **185** (1), 271 – 288.

Bruijn, R.A. De 1993 Tipstreaming of drops in simple shear flows. *Chemical Engineering Science* **48** (2), 277 – 284.

Fdhila, R. Bel & Duineveld, P.C. 1996 The effect of surfactant on the rise of a spherical bubble at high reynolds and peclet numbers. *Physics of Fluids* **8** (2), 310–321.

Hu, XY, Khoo, BC, Adams, Nikolaus A & Huang, FL 2006 A conservative interface method for compressible flows. *Journal of Computational Physics* **219** (2), 553–578.

Lauer, E., Hu, X. Y., Hickel, S. & Adams, N. A. 2012 Numerical investigation of collapsing cavity arrays. *Physics of Fluids* **24** (5).

Leal, L. G. 2004 Flow induced coalescence of drops in a viscous fluid. *Physics of Fluids* **16** (6), 1833–1851.

Luo, J., Hu, X.Y. & Adams, N.A. 2015 A conservative sharp interface method for incompressible multiphase flows. *Journal of Computational Physics* **284** (0), 547 – 565.

Matar, Omar K. & Troian, Sandra M. 1999 The development of transient fingering patterns during the spreading of surfactant coated films. *Physics of Fluids* **11** (11), 3232–3246.

Panton, R.L. 1984 *Incompressible Flow*. John Wiley & Sons Australia, Limited.

Pendse, Bhushan & Esmaeeli, Asghar 2010 An analytical solution for thermocapillary-driven convection of superimposed fluids at zero reynolds and marangoni numbers. *International Journal of Thermal Sciences* **49** (7), 1147 – 1155.

Schranner, Felix Sebastian 2017 Weakly compressible models for complex flows. PhD thesis, Technical University of Munich.

Schranner, Felix S. & Adams, Nikolaus A. 2016 A conservative interface-interaction model with insoluble surfactant. *Journal of Computational Physics* **327**, 653 – 677.

Schranner, Felix. S., Hu, Xiangyu & Adams, Nikolaus A. 2013 A physically consistent weakly compressible high-resolution approach to underresolved simulations of incompressible flows. *Computers & Fluids* **86**, 109–124.

Schranner, Felix S., Hu, Xiangyu & Adams, Nikolaus A. 2016 On the convergence of the weakly compressible sharp-interface method for two-phase flows. *Journal of Computational Physics* **324**, 94 – 114.

Teigen, Knut Erik, Song, Peng, Lowengrub, John & Voigt, Axel 2011 A diffuse-interface method for two-phase flows with soluble surfactants. *Journal of Computational Physics* **230** (2), 375 – 393.

Xu, Jian-Jun & Zhao, Hong-Kai 2003 An eulerian formulation for solving partial differential equations along a moving interface. *Journal of Scientific Computing* **19** (1-3), 573–594.

Young, N. O., Goldstein, J. S. & Block, M. J. 1959 The motion of bubbles in a vertical temperature gradient. *Journal of Fluid Mechanics* **6** (3), 350–356.